The Astrophysical Journal, 991:223 (10pp), 2025 October 1 https://doi.org/10.3847/1538-4357/adfc3e

Constrain the Hubble Constant from Extreme Mass Ratio Inspirals Dark Sirens Using Galaxy Clusters

Jian-Dong Liu[1,2], Wen-Biao Han[3,1,4,5,6], and Qianyun Yun[7]
[1] School of Fundamental Physics and Mathematical Sciences, Hangzhou Institute for Advanced Study, University of Chinese Academy of Sciences, Hangzhou 310024, People's Republic of China
[2] Institute of Theoretical Physics, Chinese Academy of Sciences, Beijing 100190, People's Republic of China
[3] Shanghai Astronomical Observatory, Chinese Academy of Sciences, Shanghai 200030, People's Republic of China; wbhan@shao.ac.cn
[4] School of Astronomy and Space Science, University of Chinese Academy of Sciences, Beijing 100049, People's Republic of China
[5] Taiji Laboratory for Gravitational Wave Universe (Beijing/Hangzhou), University of Chinese Academy of Sciences, Beijing 100049, People's Republic of China
[6] Key Laboratory of Radio Astronomy and Technology (Chinese Academy of Sciences), A20 Datun Road, Chaoyang District, Beijing, 100101, People's Republic of China
[7] School of Physics and Astronomy, Shanghai Jiao Tong University, 800 Dongchuan Road, Minhang District, Shanghai 200240, People's Republic of China
Received 2025 March 14; revised 2025 August 14; accepted 2025 August 15; published 2025 September 30

Abstract

Extreme mass ratio inspirals (EMRIs) are key observational targets for future space-based gravitational wave detectors and hold significant value in cosmological research. As a type of "standard siren," EMRIs offer an independent method to measure the Hubble constant, providing new hope for resolving the "Hubble tension" problem. However, when using the dark siren method combined with galaxy catalogs to statistically infer redshifts, EMRI events occurring in low-luminosity galaxies may not be fully recorded in the galaxy catalogs, leading to potential true hosts being missed. To address this, we propose using galaxy cluster catalogs, which contain numerous member galaxies, including faint ones, effectively reducing the risk of missing true hosts. In this study, we randomly injected three EMRI events and simulated a 2 yr observation of these events using both Laser Interferometric Space Antenna (LISA) and the joint LISA–Taiji network to demonstrate the improvements brought about by incorporating galaxy cluster catalogs into the dark siren methodology. For these three cases, compared to using galaxy catalogs alone, incorporating galaxy cluster catalogs enhanced the measurement precision of the Hubble constant to varying degrees, with a maximum improvement of approximately 41.00%. These results indicate that employing galaxy cluster catalogs in EMRI-based dark siren analyses can more effectively constrain the Hubble constant H_0.

Unified Astronomy Thesaurus concepts: Black holes (162); Gravitational waves (678); Hubble constant (758)

1. Introduction

To enhance our understanding of the Universe's evolutionary processes, it is essential to obtain more precise measurements of fundamental cosmological quantities. Currently, however, different astronomical observational methods yield inconsistent results for the Hubble–Lemaître constant H_0. For instance, the Planck experiment deduced $H_0 = 67.36^{+0.54}_{-0.54}$ km s^{-1} Mpc^{-1} (Planck Collaboration et al. 2020) based on measurements of cosmic microwave background (CMB) radiation, whereas the Supernovae, H_0, for the Equation of State of Dark Energy (SH0ES) experiment determined $H_0 = 74.03^{+1.42}_{-1.42}$ km s^{-1} Mpc^{-1} (A. G. Riess et al. 2022) by utilizing the luminosity distances and redshifts of Type Ia supernovae. This discrepancy of approximately 4.4σ (A. G. Riess et al. 2022) has resulted in what is referred to as the "Hubble tension" (W. L. Freedman 2017; A. G. Riess et al. 2021; L. Perivolaropoulos & F. Skara 2022). There are two main potential explanations for this significant discrepancy (S. M. Feeney et al. 2021): one is the model dependence of the CMB constraint, and the other is the possible existence of undiagnosed systematic errors. To address this discrepancy, an independent measurement method that does not rely on the distance ladder and achieves H_0 measurement with 1% precision is urgently needed.

After the detection of the first gravitational wave (GW) event, GW150914 (B. P. Abbott et al. 2016), LIGO/Virgo detected over 180 gravitational wave events. Gravitational waves provide a new method for measuring the Hubble constant H_0, which was initially proposed by B. F. Schutz (1986). By analyzing the GW signals emitted during the merger phase of compact binary systems, it is possible to obtain the luminosity distance from the GW source directly, without relying on a cosmic distance ladder. This is referred to as a "standard siren" (D. E. Holz & S. A. Hughes 2005; H.-Y. Chen et al. 2018a). Combining this with the corresponding redshift information allows us to infer the cosmological parameters. If redshift information can be obtained through the associated electromagnetic (EM) counterparts, this type of standard siren is referred to as a "bright siren" (B. P. Abbott et al. 2021). Notably, LIGO/Virgo first jointly detected the merger event GW170817 (B. P. Abbott et al. 2017a) of a binary neutron star (BNS) system in 2017, achieving the first measurement of the Hubble constant H_0 using standard sirens through multimessenger observations, with a result of $H_0 = 70^{+12}_{-8}$ km s^{-1} Mpc^{-1} (B. P. Abbott et al. 2017b). Although it is currently not possible to detect the EM counterparts of stellar-mass black hole mergers, we can still use statistical inference methods to obtain the corresponding redshift information, allowing us to further infer cosmological parameters. This type of standard siren is referred to as a "dark

siren" (C. L. MacLeod & C. J. Hogan 2008; H.-Y. Chen et al. 2018a; H. Leandro et al. 2022). For instance, the binary black holes (BBH) event GW170814 B. P. Abbott et al. (2017c), the Hubble constant was measured for the first time using the dark siren method in the absence of an EM counterpart, resulting in $H_0 = 75^{+40}_{-32}$ km s^{-1} Mpc^{-1} (M. Soares-Santos et al. 2019). In addition, for the gravitational wave events detected during the LIGO/Virgo O1, O2, O3, and O4a observing runs, combining well-localized dark sirens with galaxy catalogs, such as DESI, can provide more effective constraints on the Hubble constant H_0 (R. Abbott et al. 2023; W. Ballard et al. 2023; A. Palmese et al. 2023a; C. R. Bom et al. 2024; I. M. Hernandez & A. Ray 2024; F. Stachurski et al. 2024).

Future observations with next-generation ground-based detectors, such as the Cosmic Explorer (CE, D. Reitze et al. 2019) and the Einstein Telescope (ET, M. Punturo et al. 2010), are expected to detect between 10^5 and 10^6 gravitational wave events during their operational periods (N. Muttoni et al. 2023). By jointly observing the "standard siren" sources among these events, it is possible to achieve subpercentage precision measurements of the Hubble constant (N. Muttoni et al. 2023). Moreover, around 2030, a series of space detectors, such as Laser Interferometric Space Antenna (LISA; P. Amaro-Seoane et al. 2017, Taiji W.-R. Hu & Y.-L. Wu 2017, and Tianqin J. Luo et al. 2016), will be launched into orbit. These detectors are capable of detecting gravitational wave sources in the frequency range of 0.1 mHz to 1 Hz, enabling us to observe binary black hole systems composed of stellar-mass black holes, as well as extreme mass ratio inspiral (EMRIs) systems formed by supermassive black holes (SMBH) and their companion objects (CO), satisfying the mass ratio condition $q = \frac{\mu}{M} \leqslant 10^{-4}$. Here, M represents the mass of the SMBH, and μ represents the mass of the CO. EMRIs systems are an important observational source for the scientific mission of LISA and hold great potential and value in astrophysics (P. Amaro-Seoane et al. 2007; A. Klein et al. 2016, cosmology N. Tamanini et al. 2016; P. Auclair et al. 2023), and fundamental physics (E. Berti et al. 2016; S. Babak et al. 2017). D. Laghi et al. (2021) were the first to use EMRI systems as standard sirens for cosmological studies, with their results indicating that the measurement precision of the Hubble constant can reach 1.1%, demonstrating the significant potential of EMRIs as standard sirens. It is worth noting that, compared to BBH merger events, which are primarily concentrated at low redshifts, EMRI events provide an effective complement at higher redshifts, offering the prospect of measuring the Hubble constant across different redshift intervals. Moreover, with the advent of next-generation ground-based gravitational wave detectors, cross-comparing cosmological measurements obtained from both ground-based and space-based detectors within similar redshift ranges will further enhance the reliability and robustness of the results.

In this study, we conducted a brief investigation into the use of EMRIs as dark siren sources. However, due to the extreme mass ratio between the secondary object (such as a neutron star or small-mass black hole) and the supermassive black hole (MBH) in the EMRIs systems, the orbital dynamics are far more complex than in the equal-mass stellar-black hole systems, resulting in exceptionally high computational costs. This makes it very challenging to directly use the numerical relativity waveforms. Although various waveform models have been proposed for computing EMRI signals, the Analytic Kludge (AK) method (L. Barack & C. Cutler 2004) is based on quadrupole radiation on Keplerian orbits, with added general-relativistic effects such as orbital evolution caused by Lense–Thirring precession. The AK method has a simple structure and high computational efficiency; however, its limited accuracy is insufficient for precise data analysis. The Numerical Kludge (NK) method (S. Babak et al. 2007) constructs EMRI orbits using geodesics in Kerr spacetime, combined with Post-Newtonian (PN) theory, to obtain more accurate orbital-parameter evolution. However, because NK requires numerical integration at every step of the orbital evolution, its computational speed is typically about an order of magnitude slower than that of AK, which limits its application in large-scale data analyses. The Augmented Analytic Kludge (AAK) method (A. J. K. Chua et al. 2017) maps AK-model parameters to the eigenfrequencies of the NK model, effectively combining the advantages of both: under most initial parameter settings, AAK waveforms achieve over 95% overlap with NK waveforms while being about an order of magnitude faster to compute. This balance between accuracy and efficiency makes AAK particularly valuable for EMRI data analysis.

In this paper, we briefly assess the capability of using EMRIs as dark sirens, in conjunction with galaxy catalogs and galaxy cluster catalogs, to constrain the precision of the Hubble constant at redshifts $z < 0.5$. The structure of the article is as follows: In Sections 2 and 3, we provide a detailed introduction to the EMRIs waveform model used in this study, the statistical analysis methods for dark sirens, and other relevant preparations. In Section 4, we present the parameter estimation results for the LISA and LISA–Taiji networks, examine how using galaxy clusters versus galaxy catalogs affects redshift information acquisition, and assess the corresponding impact on the precision of the Hubble constant constraint. Finally, in Sections 5 and 6, we review and summarize the main findings of this study.

2. Extreme Mass Ratio Inspirals Waveforms and Data Simulation Methods

In this section, we briefly introduce the EMRIs and their waveforms, explain the waveform template we selected, and describe our method for simulating the EMRI data.

2.1. The Waveform of Extreme Mass Ratio Inspirals

The gravitational wave signal at a large distance from the source can be represented by the complex time-domain dimensionless strain, where h_+ and $h_\times$ are transverse-traceless gravitational wave polarization components (M. L. Katz et al. 2021).

$$h = h_+ - ih_\times = \frac{\mu}{d_L}\sum_{lmkn} A_{lmkn}(t) S_{lmkn}(t, \theta) e^{im\phi} e^{-i\Phi_{mkn}(t)}. \quad (1)$$

The quantity d_L is the luminosity distance of the source, t is the time of arrival of the gravitational wave at the solar system barycenter, and θ is the polar viewing angle in the source frame, ϕ is the azimuthal viewing angle in the source frame. The phase term $\Phi_{mkn} = m\Phi_\phi + k\Phi_\theta + n\Phi_r$ represents the sum of the decomposed phases for each given mode. The amplitude A_{lmkn} is related to the Teukolsky mode amplitude Z^∞_{lmkn} far from the source, and the relation is given by: $A_{lmkn} = -2Z^\infty_{lmkn}/\omega^2_{mkn}$, where $\omega_{mkn} = m\Omega_\phi + k\Omega_\theta + n\Omega_r$ is the frequency of the mode, and $\Omega_{r,\theta,\phi}$ describe the frequencies of the Kerr geodesic orbit. The function $S_{lmkn}(t, \theta)$ is the spin-weighted spherical harmonic function. The indices l, m, k, and n represent the orbital angular momentum, azimuthal momentum, polarity, and radial modes, respectively.

The parameter space of a complete EMRI waveform in the source frame consists of 15 parameters, as described by M. L. Katz et al. (2021), expressed as:

$$\{M,\ \mu,\ a,\ \boldsymbol{a}_2,\ p_0,\ e_0,\ \cos(I)_0,\ d_L,\ \theta_S,\ \phi_S,\ \theta_K,\ \phi_K,\ \Phi_{\phi,0},\ \Phi_{\theta,0},\ \Phi_{r,0}\}.$$

Here, $\{M,\ \mu,\ d_L,\ \Phi_{\phi,0},\ \Phi_{\theta,0},\ \Phi_{r,0}\}$ are defined above; $\overrightarrow{a_2}$ represents the three-dimensional spin angular momentum vector of the CO; a is the dimensionless spin parameter; p_0 is the semilatus rectum; e_0 is the eccentricity; $\cos(I)_0$ is the cosine of the inclination angle I, which describes the orbit's tilt relative to the equatorial plane; θ_S and ϕ_S are the polar and azimuthal angles describing the sky location in the solar system barycentric frame; θ_K and ϕ_K are the polar and azimuthal angles describing the orientation of the MBH's spin angular momentum vector $\hat{S}$.

Additionally, we employ `Pn5AAKWaveform` as the waveform model. This model analytically integrates the orbital parameters using the 5PN radiation dissipation formula and directly computes and interpolates the fundamental frequencies $\{\Omega_r, \Omega_\theta, \Omega_\phi\}$ along the orbit. This approach eliminates the need for the traditional AAK method's mapping from the physical parameter set (M, a, p) to the nonphysical parameter set $(\tilde{M}, \tilde{a}, \tilde{p})$. Specifically, after obtaining the fundamental frequencies through orbital evolution, the phase evolution is constructed via

$$\dot{\Phi} = \Omega_r, \quad \dot{\gamma} = \Omega_\theta - \Omega_r, \quad \dot{\alpha} = \Omega_\phi - \Omega_\theta. \tag{2}$$

Compared to the conventional AAK approach, this method significantly enhances the waveform generation speed and overall efficiency while maintaining high phase accuracy.

2.2. Simulation of Gravitational Wave Data

2.2.1. Bayesian Inference

For a known form of the power spectral density (PSD), we can define the gravitational wave likelihood function $\mathcal{L}$.

$$\ln \mathcal{L} = -\frac{1}{2}\langle d - \theta | d - \theta \rangle. \tag{3}$$

Here, d is the strain data, and θ is the set of parameters to be inferred. We have introduced the noise-weighted inner product:

$$\langle a|b\rangle = 4Re\left[\int_0^\infty \frac{\tilde{a}(f)\,\tilde{b}^*(f)}{S_n(f)}\,df\right]. \tag{4}$$

Here, $\tilde{a}(f)$ is the Fourier transform of $a(t)$, and $S_n(f)$ is the PSD of the noise. The signal-to-noise ratio (SNR) of the signal can then be computed as $\rho = \sqrt{\langle d|h\rangle}$. When ρ is greater than 15, we consider the event to be detected. In this simulation, the injection parameters of the three events were randomly drawn from the uniform prior ranges listed in Table 1. The signals were injected into the Gaussian noise generated by the design sensitivities of LISA and Taiji, and we used the Eryn sampler to generate the posterior distribution of the data.

3. Cosmological Models and Standard Sirens

In this section, we introduce the cosmological model used and explain how to calculate the Hubble constant using dark sirens.

Table 1
The Prior Range of Some Parameters of Extreme Mass Ratio Inspirals

Parameter	Prior Range	Description
μ	$10-20M_\odot$	CO mass
a	0.9–0.99	MBH spin
p_0	9–16	Semilatus rectum
e_0	0–0.4	Orbital eccentricity
$\cos(I)_0$	[−1, 1]	Inclination cosine
d_L	0–7Gpc	Luminosity distance
ϕ_S	$0-2\pi$	R.A. (azimuthal angle)
θ_S	$0-\pi$	decl. (polar angle)

Note. The prior ranges of the selected parameters are presented in this table. Additionally, we fixed the values of the following parameters: $M = 10^6 M_\odot$, $\Phi_{\phi,0} = 2.0$, $\Phi_{\theta,0} = 3.0$, and $\Phi_{r,0} = 4.0$.

3.1. ΛCDM Cosmological Model

In this study, we adopted the flat ΛCDM model as the base model, with the expansion of the Universe characterized by the Hubble–Lemaître parameter $H(z)$:

$$H(z) = H_0\sqrt{\Omega_m(1+z)^3 + 1 - \Omega_m} \tag{5}$$

where the EoS parameter w for dark energy is assumed to be -1, and Ω_m is the current matter density parameter (J. A. Frieman et al. 2008). The fiducial values of the remaining cosmological parameters used in the simulation were chosen on the basis of the Planck 2018 results (Planck Collaboration et al. 2020), including TT, TE, EE + lowE data, where $\Omega_m = 0.3166$ and $H_0 = 67.27^{+0.60}_{-0.60}$ km s^{-1} Mpc^{-1}.

In addition, the luminosity distance of the source at redshift $d_L(z)$ is given by the following formula:

$$d_L(z) = c(1+z)\int_0^z \frac{dz'}{H(z')}, \tag{6}$$

where c is the speed of light and $H(z)$ is the Hubble parameter describing the expansion rate of the Universe at redshift z.

3.2. Dark Sirens Statistical Framework

3.2.1. Galaxy Localization with Catalogs

The key to inferring cosmological parameters using gravitational wave dark standard sirens lies in obtaining the corresponding redshift information from galaxy catalogs. In this study, we adopt data from the DESI (Z. L. Wen & J. L. Han 2024) survey and the simulated CSST (Y. Gu et al. 2024) survey as the sources for our galaxy and galaxy cluster catalogs. The DESI catalog covers approximately 19,700 square degrees of the sky, while the CSST catalog is expected to cover about 17,500 square degrees. When performing parameter inference using galaxy catalogs, selecting an appropriate apparent magnitude cut is crucial.

The study by V. Alfradique et al. (2025) showed that, in the low to intermediate redshift range, using a brighter magnitude threshold (e.g., $m_r < 20$) can lead to a bias in the posterior distribution of the Hubble constant H_0, shifting the peak toward lower values. In contrast, adopting a more relaxed threshold (e.g., $m_r < 21$ or $m_r < 22$) maintains a high level of catalog completeness (approximately 86%–99%), resulting in low impact on the final inference. In this study, we adopt $m_z < 21$ as the apparent magnitude cut. Compared to $m_r < 21$, this choice ensures better completeness of the catalog at intermediate

redshifts within the range $0 < z < 0.5$, thereby improving the reliability of host galaxy identification. For the galaxy sample, when applying a magnitude cut of $m_z < 21$, the galaxy catalog exhibits high completeness (Y. Gu et al. 2024) and therefore does not introduce Malmquist bias. Therefore, we do not apply any correction for catalog incompleteness in the subsequent analysis. Given that the central black hole mass was set to $10^6\,M_\odot$, and such black holes have been observed in galaxies with stellar masses in the range $10^9\,M_\odot < M_* < 10^{11}\,M_\odot$ (A. E. Reines & M. Volonteri 2015), we selected galaxies with stellar masses $M_* > 10^9 M_\odot$ as our analysis sample. Under this selection criterion, galaxies satisfying $M_* > 10^9 M_\odot$ account for 96.74% and 95.05% of the total number of galaxies in the CSST and DESI catalogs, respectively. Although this selection increases the number of potential host galaxies within each localization volume (D. Laghi et al. 2021), it also helps avoid missing low-mass host systems. For galaxy clusters, we selected systems with stellar masses $M_* > 10^{13} M_\odot$ to avoid missing low-mass clusters (Z. L. Wen & J. L. Han 2024). In the subsequent analysis, we adopt photometric redshifts for the calculations. Although their precision is lower than that of spectroscopic redshifts, photometric observations can cover a much larger galaxy sample, thereby effectively reducing the risk of missing the true host galaxy. For galaxies, we adopt a typical photometric redshift uncertainty of $0.03(1+z)$, while for galaxy clusters, the redshift uncertainty is generally lower than that of individual galaxies due to the presence of multiple member galaxies. Previous studies have provided an empirical value of $0.01(1+z)$ (E. S. Rykoff et al. 2016). In this work, we adopt a relatively conservative estimate of the redshift uncertainty with the specific calculation formula given below:

$$\sigma_z = \begin{cases} 0.03(1+z_s), & \text{for Galaxy} \\ 0.013(1+z_s), & \text{for Cluster} \end{cases}. \tag{7}$$

Here, z_s represents the spectroscopic redshift of the cluster. In addition to the uncertainty arising from the redshift measurement itself, the peculiar velocity of the galaxy during the observation period introduces additional redshift errors. Therefore, we incorporate this systematic effect into the total redshift uncertainty, as shown below:

$$\sigma_z^{\rm tot} = \sqrt{(\sigma_z)^2 + (\sigma_z^{\rm PV})^2}. \tag{8}$$

Here, σ_z is the standard deviation of the redshift, $\sigma_{z^{\rm PV}(z)}$ represents the peculiar velocity error, given by S.-J. Jin et al. (2023)

$$\sigma_z^{\rm PV}(z) = (1+z)\frac{\sqrt{\langle v^2\rangle}}{c}, \tag{9}$$

where $\sqrt{\langle v^2\rangle}$ is the velocity error of the galaxies, which we assumed to be 500 km s^{-1}.

The host galaxy of a GW source can be statistically identified by crossmatching a three-dimensional localization volume with galaxy catalogs. This localization volume is jointly determined by the uncertainty in the luminosity distance and the localization error of the GW detector. Specifically, based on the luminosity distance d_L and its statistical uncertainty Δd_L inferred from the GW signal, the source's possible radial distribution can be constrained within the interval: $[d_{\rm min},\ d_{\rm max}] = [d_L - 2\,\Delta d_L,\ d_L + 2\,\Delta d_L]$. By combining the flat prior $H_0 \in [20, 140]$ km s^{-1} Mpc^{-1}, and assuming the ΛCDM model, this distance interval can be translated into a corresponding redshift range via the distance–redshift relation given in 5 and 6: $\Delta z = [z_{\rm min},\ z_{\rm max}]$.

In addition, the directional information encoded in the GW signal, namely the R.A. θ and decl. ϕ constrains the sky position of the source. By combining the radial and angular constraints, a three-dimensional localization volume can be constructed, within which potential host galaxies may reside. The angular separation between each galaxy in this volume and the GW source can be characterized by a 2×2 covariance matrix, given by the following expression (S.-J. Jin et al. 2023):

$$\chi^2 = (\theta - \bar{\theta},\ \phi - \bar{\phi})\,{\rm Cov}[\theta,\ \phi]^{-1}(\theta - \bar{\theta},\ \phi - \bar{\phi})^T. \tag{10}$$

Here, θ and ϕ represent the two angular coordinates (R.A. and decl.) of an arbitrary potential host galaxy, while $\bar{\theta}$ and $\bar{\phi}$ represent the two angular coordinates of the gravitational wave source. When the galaxies within the selected region satisfy $\chi^2 \leqslant 9.21$, they correspond to the 99% confidence level. These galaxies are considered potential host galaxies of the gravitational wave source.

3.2.2. Inferring Cosmological Parameters through Dark Sirens

We follow the method proposed by H.-Y. Chen et al. (2018b), combining the gravitational wave data $d_{\rm GW}$ and electromagnetic data $d_{\rm EM}$ from galaxy catalogs, and apply Bayes' theorem to infer the cosmological parameter H_0. The posterior distribution can be written as:

$$p(H_0|d_{\rm GW},\, d_{\rm EM}) \propto p(d_{\rm GW},\, d_{\rm EM}|H_0)p(H_0), \tag{11}$$

where $p(H_0)$ is the uniform prior distribution of H_0, and $p(d_{\rm GW},\, d_{\rm EM}|H_0)$ is the likelihood. Next, since the gravitational wave data and the electromagnetic data are independent, the numerator in Equation (11) can be factorized into two parts: one corresponding to the likelihood of the gravitational wave data and the other to that of the electromagnetic data. Next, we marginalize the remaining nuisance parameters. Given LISA's good localization capability for gravitational wave events, we do not consider the impact of localization on the posterior results in the likelihood function for the gravitational wave data. Finally, we obtain the marginalized likelihood function:

$$\begin{aligned} & p(d_{\rm GW},\, d_{\rm EM}|H_0) \\ &= \frac{1}{\beta(H_0)}\int p(d_{\rm GW},\, d_{\rm EM}|H_0,\, z,\, \Omega_{\rm EM},\, D_L,\, \Omega_{\rm GW}) \\ &\quad \times p(\Omega_{\rm GW})p(D_L)p(z)p(\Omega_{\rm EM}) \\ &\quad \times dD_L\, d\Omega_{\rm GW}\, d\Omega_{\rm EM}\, dz \\ &= \frac{1}{\beta(H_0)}\int p(d_{\rm GW}|D_L,\, \Omega_{\rm GW})\; p(d_{\rm EM}|z,\, \Omega_{\rm EM}) \\ &\quad \times \delta(D_L - \hat{D}_L(z,\, H_0))\delta(\Omega_{\rm GW} - \Omega_{\rm EM}) \\ &\quad \times p(z,\, \Omega_{\rm EM}|H_0)dD_L\, d\Omega_{\rm GW}\, d\Omega_{\rm EM}\, dz \\ &= \frac{1}{\beta(H_0)}\int p(d_{\rm GW}|\hat{D}_L(z,\, H_0)) \\ &\quad \times p(d_{\rm EM}|z,\, \Omega_{\rm EM}) \\ &\quad \times p(z,\, \Omega_{\rm EM}|H_0)\; d\Omega_{\rm EM}\, dz, \end{aligned} \tag{12}$$

where δ is the Dirac delta function. Meanwhile, $p(d_{\rm GW}|\hat{D}(z,\, H_0))$ denotes the marginalized gravitational wave likelihood, as defined

in Equation (13).

$$p(d_{\rm GW}|\hat{D}_L(z, H_0)) = \frac{1}{\sqrt{2\pi}(\sigma_{d_L})}\exp\left(-\frac{(d_L - \hat{D}_L(z, H_0))^2}{2(\sigma_{d_L})^2}\right). \tag{13}$$

The marginal electromagnetic likelihood $p(d_{\rm EM}|z, \Omega)$ can be computed as prescribed in Equation (14).

$$p(d_{\rm EM}|z, \Omega_{\rm EM}) = \frac{1}{N}\sum_{i=1}^{N}\omega_i \frac{1}{\sqrt{2\pi}\sigma_z(z_i)}\exp\left(-\frac{(z_i - z)^2}{2\sigma_z^2(z_i)}\right)\frac{dV_c}{dz}. \tag{14}$$

Here, ω_i is the angular localization weight for each potential host galaxy, given by the following expression:

$$\omega_i \propto \exp\left(-\frac{1}{2}\chi^2\right). \tag{15}$$

Here, i denotes the index of a potential host galaxy, ω_i represents the angular weight of the ith potential host galaxy. The chi-squared statistic χ^2 is defined in Equation (10). And V_c represents the comoving volume.

Finally, we marginalize over the redshift and sky position of the galaxies. Assuming that the galaxies are uniformly distributed in comoving volume and that the catalog covers a maximum volume of $V_{\rm max}$, we have:

$$\begin{aligned} p(z, \Omega_{\rm EM})d\Omega_{\rm EM}\, dz &\propto \frac{1}{V_{\rm max}}\frac{d^2V}{d\Omega_{\rm EM}\, dz}d\Omega_{\rm EM}\, dz \\ &\propto \frac{1}{V_{\rm max}}\frac{r^2(z)}{H(z)}d\Omega_{\rm EM}\, dz. \end{aligned} \tag{16}$$

Finally, to correct for the selection effects on the GW events and galaxies introduced by the experimental sensitivity and detection pipelines, we consider the normalization factor $\beta(H_0)$, which is used to normalize the likelihood over all possible GW and EM data. The explicit form of this factor is given in Equation (17), and its derivation is provided in Appendix A.

$$\beta(H_0) \approx \frac{V[d_{L,\rm GW}^{\rm max}(H_0)]}{V_{\rm max}(H_0)}. \tag{17}$$

Here, $V[d_{L,\rm GW}^{\rm max}(H_0)]$ represents the largest volume within which the considered GW events can be observed.

Based on the above formulas, a Monte Carlo analysis was performed to obtain the results for the EMRIs data and the Hubble constant. Given that most EMRI events can remain within the LISA's detection band for several months to years (P. Amaro-Seoane et al. 2017), we injected three EMRI events and simulated 2 yr of observations of these events using the joint LISA and LISA–Taiji detector network (detailed information can be found in Appendix B). Long-duration observations help accumulate higher SNR, thereby improving the precision of the intrinsic parameter estimation for the sources. In addition, to quantify the difference between the two probability distributions of priors and estimated results, we employ the Hellinger distance. The Hellinger distance between two distinct probability distributions P and Q is defined as: $\text{Hellinger}(P, Q) = \sqrt{1 - \sum_i \sqrt{p_i \cdot q_i}}$ (E. Hellinger 1909; H. Leandro et al. 2022). This metric measures the similarity between probability distributions. In this context, P and Q represent the prior and posterior distributions of a certain parameter, respectively. In these distributions, p_i and q_i denote different sample points.

4. Analysis Results of Different Galaxy and Galaxy Cluster Catalogs

In this section, we present our analysis results, including the posterior distribution of the luminosity distance and the sky localization results for the simulated EMRI events, the posterior distribution of the redshift obtained using the galaxy catalogs and galaxy cluster catalogs, and the constraints on the Hubble constant based on the galaxy and cluster catalogs.

4.1. Parameter Estimation Results and Sky Localization

Figure 1 presents the posterior distributions of the luminosity distances for LISA and LISA–Taiji joint detection. The violin plots show the estimates obtained by the two methods at different luminosity distances. The estimated accuracy is 0.40% $\sim$ 0.73% when considering only the LISA detector. However, when considering the LISA–Taiji joint detection, the accuracy improves by a factor of 3–8 compared to the former. In addition, we compute the Hellinger distance to quantify the difference between the prior and posterior distributions. The upper panel of Figure 1 shows the Hellinger distance at different luminosity distances. However, as the luminosity distance increases, the relative error in the results also increases.

In addition, we calculated the sky localization accuracy after 2 yr of observation by LISA or LISA–Taiji. As shown in Figure 2, we present the sky localization results for LISA. The results indicate that, within the 90% confidence interval, the sky localization area ranges from 3 to 6 deg^2. Such localization precision is sufficient to significantly reduce the number of potential host galaxies and improve the statistical identification of the host, thereby facilitating the measurement of redshift information. Furthermore, we also computed the sky localization regions for these three events under joint LISA–Taiji observations and found that their localization areas are all less than 1 square degree. This will significantly reduce the number of galaxies within the localization volume, helping to minimize contamination from unrelated galaxies.

4.2. Redshift Posterior Distribution Analysis of the Galaxy and Galaxy Cluster Catalogs

Figure 3 shows the redshift probability distribution of the host galaxies within the three-dimensional localization volume, computed using different types of galaxy catalogs. The probability weight w_j for each galaxy is calculated according to Equation (15). The results indicate that using a galaxy cluster catalog enables more effective identification of the true host galaxy, the main reasons are as follows: first, within the three-dimensional localization volume we analyze, a standard galaxy catalog typically contains thousands of candidate hosts, whereas a cluster catalog, due to its lower spatial density, usually includes only a few hundred candidates, thereby substantially reducing contamination from nonhost galaxies. Even at high redshift, when uncertainties in luminosity distance and sky localization jointly inflate the localization volume, the cluster catalog still effectively identifies the host. Second, because standard galaxy catalogs are limited by observational depth (e.g., magnitude thresholds), they tend to miss faint hosts, which

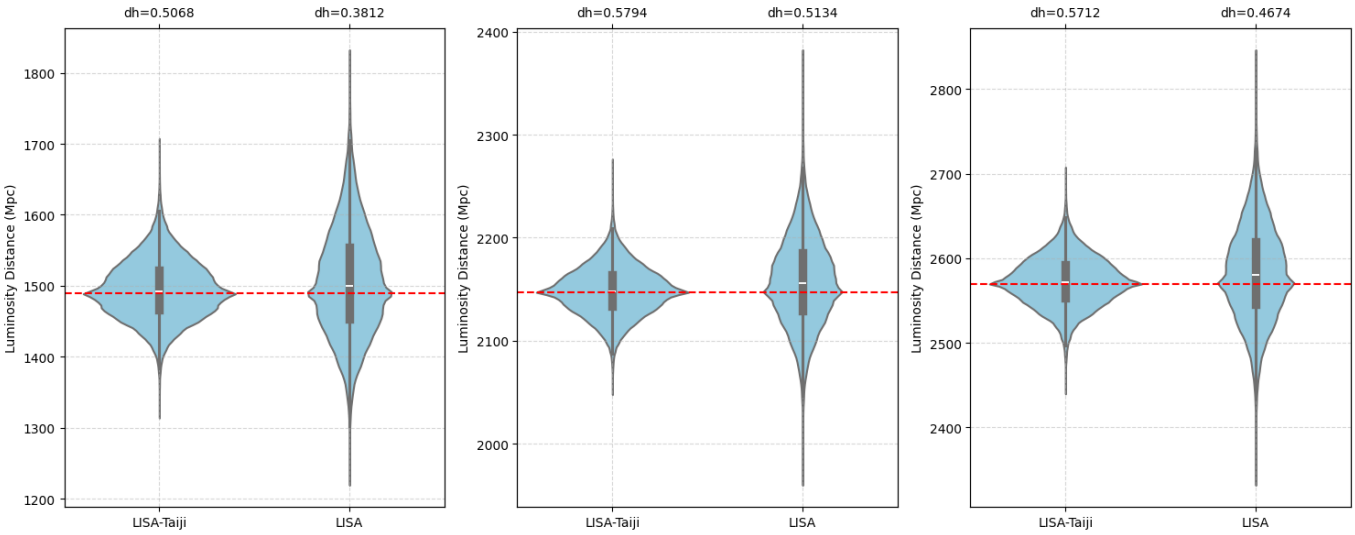

Figure 1. Posterior distribution of the luminosity distance at different injection distances. The red line in each subplot indicates the injection distance, presented from left to right. The left side of each subplot shows the results from the joint LISA–Taiji observation, while the right side presents the results from the LISA observation. The value at the top, *dh*, corresponds to the Hellinger distance for each result.

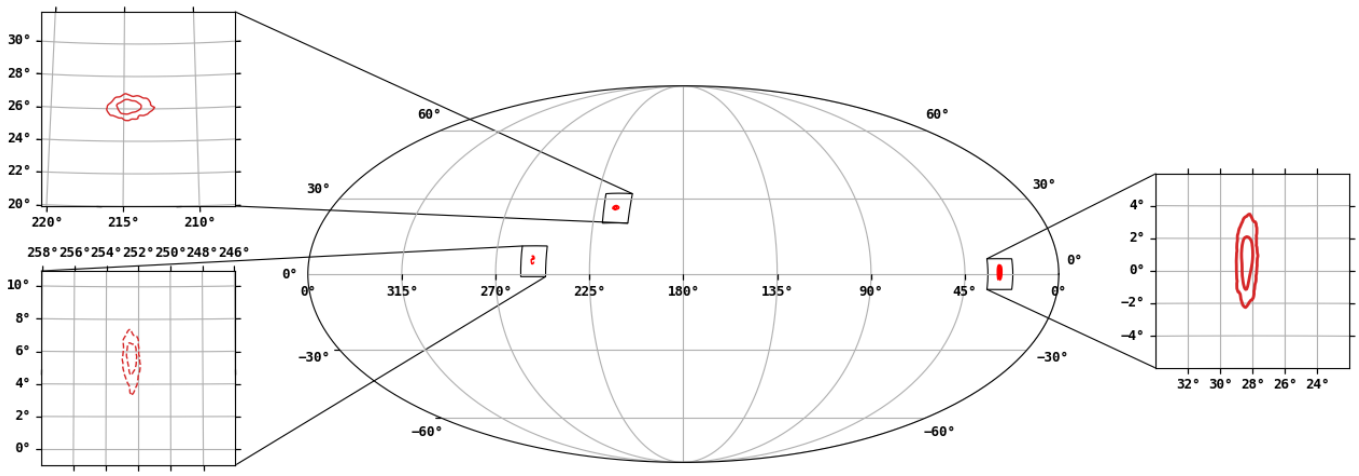

Figure 2. Source localization results based on simulated LISA 2 yr observation data. The plot shows the sky localization range within the 50% and 90% confidence intervals.

are then systematically downweighted or omitted in the probability assignment. In contrast, a cluster catalog can indirectly incorporate these undetected faint members through the statistical properties of the cluster as a whole, thereby mitigating the bias introduced by host nondetection.

4.3. Constraints on the Precision of the Hubble Constant

In Figure 4, we present the impact of selecting either galaxy catalogs or galaxy cluster catalogs on the constraint precision of the Hubble constant using the dark siren method. Considering observations by LISA, the H_0 constraint precision achieved using the DESI and CSST galaxy catalogs is 18.56% and 20.16%, respectively; by contrast, when galaxy cluster catalogs are employed, the precision is significantly improved to 10.95% and 12.97%, respectively. Additionally, we consider the case of joint LISA–Taiji observations, finding that the precision on H_0 constraints using galaxy cluster catalogs ranges from 5.10% to 7.61%. In addition, we further evaluated the impact of the redshift uncertainties for galaxies and galaxy clusters on the final results. Assuming the same redshift uncertainty for galaxy clusters as for galaxies, using galaxy cluster catalogs yields an improvement in the precision of approximately 12.56%–24.14% compared to galaxy catalogs.

The reasons for the improved precision offered by galaxy cluster catalogs are as follows: first, the number density of galaxy clusters is much lower than that of individual galaxies, significantly reducing the number of potential host candidates within the sky localization volume and thus decreasing the uncertainty from statistical association. Second, galaxy clusters can include galaxies that are often missed in galaxy surveys, particularly when EMRI events occur in relatively faint or distant galaxies. This advantage is especially important for ensuring that potential host galaxies are not overlooked. Ultimately, because galaxy clusters consist of numerous member galaxies, their combined redshift measurements exhibit significantly higher precision than those of individual galaxies, thereby substantially reducing redshift uncertainties and tightening the constraints on the Hubble constant. Therefore, matching EMRI events to galaxy clusters rather

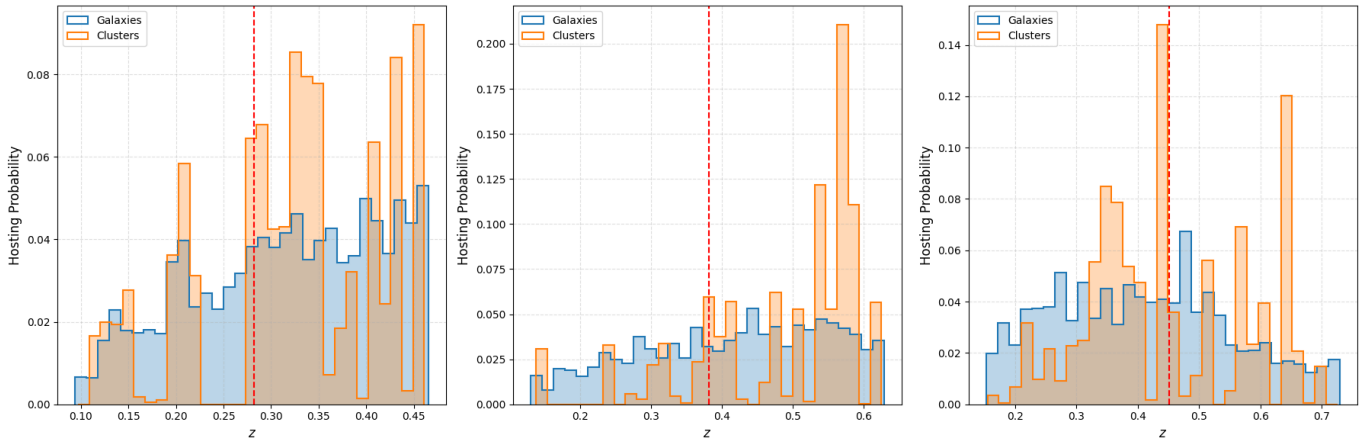

Figure 3. The figure shows the redshift probability distributions of the host galaxies within the three-dimensional localization volume using different types of catalogs. The orange curve corresponds to the results based on the galaxy cluster catalog, while the blue curve corresponds to those based on the galaxy catalog. In each panel, the red dashed line indicates the redshift of the true injected host galaxy.

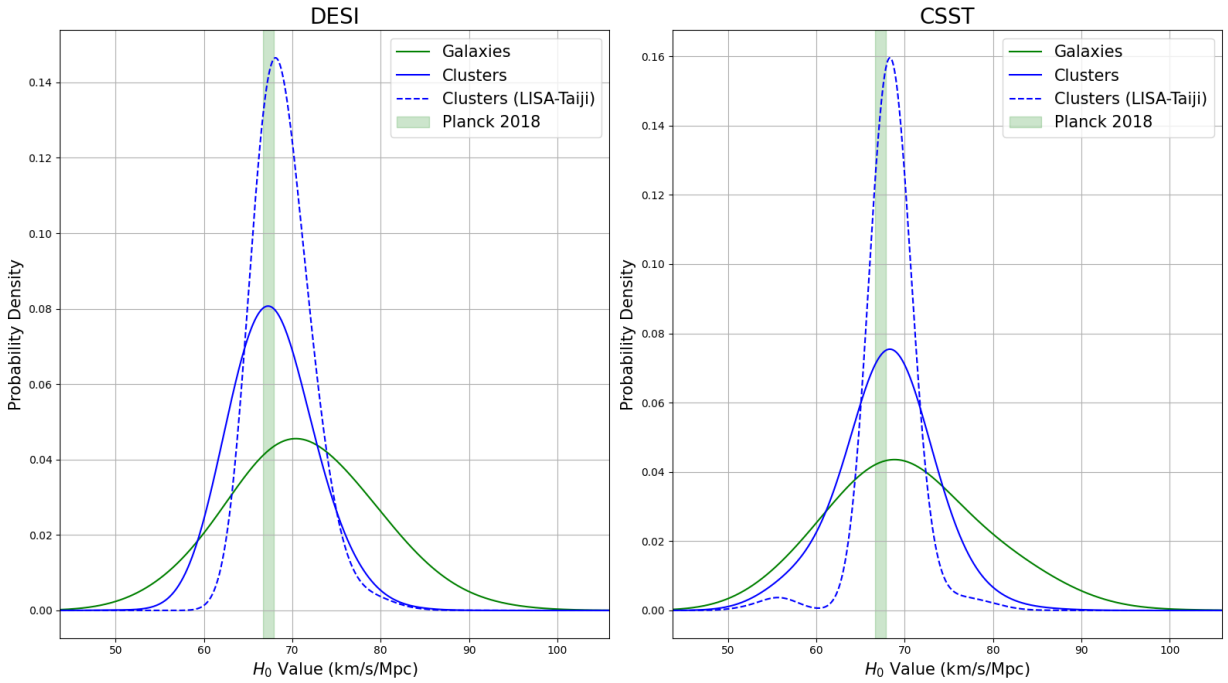

Figure 4. A comparison of the H_0 results inferred using galaxy catalogs and galaxy cluster catalogs in the dark siren method. The green solid line represents the results based on galaxies, the blue solid line represents the results based on galaxy clusters, and the blue dashed line represents the results obtained using galaxy clusters under joint observation. The green shaded region corresponds to the 90% confidence interval of the Planck 2018 measurements.

than to individual galaxies allows for the acquisition of more reliable redshift information, thereby enhancing the accuracy and credibility of cosmological inference.

Table 2 summarizes the estimation results of the Hubble constant H_0 and the corresponding constraint precision. The table labels the three injected events as EMRI 1, EMRI 2, and EMRI 3, with each row presenting the inferred H_0 results based on different types of galaxy catalogs for the corresponding event. Overall, for a single event observed by LISA over a 2 yr period, using statistical redshift information from galaxy cluster catalogs improves the measurement precision of the Hubble constant H_0 by approximately 41.00%, 34.68%, and 32.25% compared to using galaxy catalogs alone. Additionally, a 2 yr joint observation by LISA and Taiji can achieve about 5% precision in constraining H_0, further emphasizing the importance of prioritizing galaxy cluster catalogs in cosmological studies employing EMRIs as dark sirens.

5. Discussions

5.1. The Advantages of Using Galaxy Cluster Catalogs in Dark Sirens Method

It is well known that sky surveys are generally more sensitive to nearby and brighter galaxies, whereas distant or faint galaxies are often underrepresented. Consequently, if an EMRI occurs in a faint or distant galaxy, the redshift inferred through statistical methods may suffer not only from statistical uncertainty but also from additional systematic bias.

Table 2
Summary of Main Results

DESI	LISA				LISA–Taiji	
	Galaxy		Cluster		Cluster	
	H_0 (km s^{-1} Mpc^{-1})	$\Delta H_0/H_0$	H_0 (km s^{-1} Mpc^{-1})	$\Delta H_0/H_0$	H_0 (km s^{-1} Mpc^{-1})	$\Delta H_0/H_0$
EMRI 1	$70.90^{+13.69}_{-12.62}$	18.56%	$67.58^{+8.13}_{-6.67}$	10.95%	$68.57^{+5.92}_{-3.96}$	7.21%
EMRI 2	$67.88^{+10.35}_{-9.11}$	14.34%	$68.45^{+5.64}_{-6.70}$	9.02%	$68.23^{+5.30}_{-4.77}$	7.37%
EMRI 3	$68.75^{+9.27}_{-8.47}$	12.90%	$68.14^{+6.01}_{-5.90}$	8.74%	$67.88^{+7.37}_{-1.78}$	6.74%
CSST	LISA				LISA–Taiji	
	Galaxy		Cluster		Cluster	
	H_0 (km s^{-1} Mpc^{-1})	$\Delta H_0/H_0$	H_0 (km s^{-1} Mpc^{-1})	$\Delta H_0/H_0$	H_0 (km s^{-1} Mpc^{-1})	$\Delta H_0/H_0$
EMRI 1	$69.62^{+15.64}_{-12.41}$	20.16%	$68.11^{+8.01}_{-9.66}$	12.97%	$68.38^{+3.72}_{-3.26}$	5.10%
EMRI 2	$68.37^{+9.95}_{-8.46}$	13.47%	$67.36^{+7.14}_{-6.55}$	10.16%	$67.47^{+4.99}_{-5.28}$	7.61%
EMRI 3	$68.80^{+7.42}_{-8.36}$	11.46%	$68.16^{+6.84}_{-4.84}$	8.57%	$67.54^{+5.72}_{-4.54}$	7.60%

Note. For three EMRI events, we infer the Hubble constant H_0 using the dark siren method, based on 2 yr of joint observations from LISA and the LISA–Taiji network, in combination with both galaxy and galaxy cluster catalogs. The upper part of the table presents the results obtained using the DESI catalogs, while the lower part shows those based on the CSST catalogs. All results are calculated using the 90% confidence interval.

In comparison, utilizing galaxy cluster catalogs can significantly alleviate this issue. Studies of faint galaxies have shown that a large number of low-luminosity dwarf galaxies are missed by standard surveys, even within nearby galaxy clusters, suggesting that traditional observations may systematically underestimate the number of cluster members (M. P. Ulmer et al. 2011; A. Venhola et al. 2021). Since galaxy clusters typically contain both bright and faint member galaxies, even if an EMRI event occurs in a faint galaxy that is not individually detected, it may still be indirectly identified through the statistical properties of its host cluster, thereby effectively reducing the risk of missing the true host galaxy. Moreover, within a localized three-dimensional volume, Standard galaxy catalogs typically contain many galaxies, resulting in nonzero weights being assigned to nearly all candidate host galaxies. This leads to broader posterior distributions for the cosmological parameters (A. Palmese et al. 2023), i.e., increased uncertainties. In contrast, the number of galaxy clusters is much smaller than that of individual galaxies, which enhances the statistical identification of the true host and effectively reduces contamination from unrelated galaxies. Finally, due to the significantly lower redshift measurement uncertainty of galaxy clusters compared to individual galaxies (E. S. Rykoff et al. 2016), the propagation of uncertainties in the analysis is effectively reduced, thereby enhancing the precision and reliability of the constraints on the final results. Nevertheless, it should be noted that different galaxy cluster identification algorithms can significantly affect the number and properties of the clusters in the final catalog. In constructing their cluster sample, Z. L. Wen & J. L. Han (2024) adopted a method that combines the identification of the brightest cluster galaxy (BCG) with color nearest-neighbor techniques. This approach may result in the omission of clusters located in edge regions or with low richness or in the erroneous merging of such clusters into nearby, richer systems. Our preliminary assessment suggests that this issue could introduce a systematic bias of approximately 0.2% in the final results. In addition, the redshift of a galaxy cluster may deviate from the true redshift of its host galaxy, which also constitutes a source of systematic error. As these issues are beyond the scope of the present study, we do not explore them further here. Addressing these systematic biases will be an important direction for future research.

5.2. In Comparison with Current Existing Results

Several studies have investigated using EMRIs as standard sirens. C. L. MacLeod & C. J. Hogan (2008) showed that at redshift $z \approx 0.5$, accumulating around 20 EMRI events could improve the precision on H_0 to roughly 1%, but their analysis relied on idealized assumptions (e.g., equal weights for all galaxies within the localization volume, only approximate relations used) and did not involve detailed parameter estimation, serving mainly as a methodological proof of concept.

D. Laghi et al. (2021) were the first to systematically apply the Fisher matrix approach to assess the cosmological potential of EMRI dark sirens. In their fiducial model M1, for events with SNR > 100, a 4 yr observation can constrain the Hubble constant H_0 to approximately 2.5% precision, while extending the observation to 10 yr can further improve this to about 1.5%. Moreover, the uncertainty in H_0 scales roughly as $1/\sqrt{N}$ with the number of events N (B. F. Schutz 1986). Based on this empirical relation, we compare our results to those predictions by D. Laghi et al. (2021). For a single event using only a galaxy catalog, our constraint on H_0 is slightly less precise than theirs for two main reasons: first, our analysis considers only a 2 yr observation, resulting in a lower average SNR; second, as noted in Section 3.2.1, we impose a stellar-mass threshold of $M_* > 10^9 M_\odot$ for galaxies, which increases the number of candidate hosts in the localization volume and produces more peaks in the redshift dimension of the host probability distribution, thereby slightly reducing the final precision.

In addition, L.-G. Zhu et al. (2024), under the assumption that all EMRI events originate from active galactic nuclei (AGN), investigated the feasibility of constraining cosmological

parameters using an AGN galaxy catalog. They found that with 5 yr of observations by the TianQin detector, the Hubble constant H_0 could be constrained to about 3%–8%. However, according to estimates by Z. Lyu et al. (2025), EMRI–AGN systems account for only about 1%–10% of all EMRI events, which limits the applicability of this approach.

6. Conclusions

In this article, we investigated the impact of selecting different types of catalogs (galaxy catalogs versus galaxy cluster catalogs) on the precision of cosmological parameter constraints within the dark siren framework.

Initially, we applied Bayesian inference to evaluate the parameter estimation accuracy of the luminosity distance, R. A., and decl. based on 2 yr observations of EMRI events with LISA and the LISA–Taiji network. A comparative analysis of the results is presented in Section 4.1. Building upon this, we further calculated the three-dimensional localization volumes corresponding to EMRI events and, by combining data from the DESI survey and simulated CSST survey, provided the probability distribution of host galaxies in redshift within the localization volumes. Because the number of galaxy clusters is significantly smaller than that of individual galaxies, the analysis based on galaxy cluster catalogs effectively reduces the statistical errors caused by the excessive number of candidate galaxies. However, as the source luminosity distance increases, two challenges arise. On the one hand, the uncertainties in the luminosity distance and sky localization also increase, leading to a significant expansion of the three-dimensional localization volume, thereby encompassing more unrelated galaxies and introducing additional statistical uncertainties when associating the true host galaxy. On the other hand, the completeness of the galaxy catalogs decreases with distance, as fainter and more distant galaxies may be missed, increasing the risk of overlooking the true host. In contrast, galaxy cluster catalogs, which include both bright and faint galaxies within clusters, can effectively mitigate the problem of missing faint host galaxies. Finally, based on the preceding analysis, we further investigate the impact of using different catalogs on the precision of the Hubble constant inference via the dark siren method under joint observation scenarios. The results show that using galaxy cluster catalogs improves the constraint precision on the Hubble constant by up to 41.00% compared to using galaxy catalogs. Therefore, in studies employing dark sirens to infer the Hubble constant, prioritizing the use of galaxy cluster catalogs will further enhance the accuracy and reliability of the results.

In the future, with the continued operation of LISA and Taiji, along with the expansion of more survey projects, we will obtain more EMRI events at different redshifts and more comprehensive galaxy catalogs, leading to more accurate results. Through LISA–Taiji joint observations, we will be able to detect gravitational wave sources at higher redshifts, allowing us to use EMRIs as cosmological probes to study the evolution of the Universe at different redshifts. During the operation of space-based gravitational wave detectors, combining multiple high-precision events is expected to improve the measurement accuracy of cosmological parameters to the subpercent level, providing strong support for resolving the "Hubble tension."

Acknowledgments

This work was supported by the National Key R&D Program of China (grant No. 2021YFC2203002), and the National Natural Science Foundation of China (grant Nos. 12473075 and 12173071). This work made use of the High-Performance Computing Resource in the Core Facility for Advanced Research Computing at Shanghai Astronomical Observatory.

Software: FastEMRIsWaveforms (A. J. K. Chua et al. 2021; M. L. Katz et al. 2021, 2023b), Fastlisaresponse (M. L. Katz et al. 2022; M. Katz et al. 2024), LISAanalysistools (M. Katz et al. 2024), Eryn (D. Foreman-Mackey et al. 2013; N. Karnesis et al. 2023; M. Katz et al. 2023a), Cupy (R. Okuta et al. 2017), astropy (T. P. Robitaille et al. 2013; Astropy Collaboration et al. 2018, 2022), Scipy (P. Virtanen et al. 2020).

Appendix A
Derivation of β_0

H.-Y. Chen et al. (2018b) first proposed a method for calculating β_0 under the assumption that galaxies are uniformly distributed in comoving volume. This calculation is restricted to a monochromatic population of sources. In this case, the detection model can be simplified as (A. Finke et al. 2021):

$$p_{\rm det}^{\rm GW}(d_L) = \int d\Omega\, p_{\rm det}^{\rm GW}(d_L, \hat{\Omega}) = \theta(d_{\rm max} - d_L),$$

where θ denotes the Heaviside step function, and $d_{\rm max}$ represents the maximum luminosity distance at which this type of GW source can be detected, given the sensitivity of the detector network. Furthermore, using Equations (5) and (6), one can derive the maximum redshift $z_{\rm max}$ corresponding to $d_{\rm max}$, thereby rewriting the detection model in terms of redshift as:

$$p_{\rm det}^{\rm GW}(z; H_0) = \theta[z_{\rm max}(H_0; d_{\rm max}) - z].$$

Based on the above assumptions, we can finally obtain:

$$\begin{aligned}\beta(H_0) &= \int p_{\rm det}^{\rm GW}(\hat{D}_L(z, H_0), \Omega)\, p_0(z, \Omega)\, d\Omega\, dz \\ &= \frac{1}{V_{\rm max}} \int \theta[z_{\rm max}(H_0; d_{\rm max}) - z]\, \frac{r^2(z)}{H(z)}\, d\Omega\, dz \\ &\approx \frac{V[d_{L,\rm GW}^{\rm max}]}{V_{\rm max}}.\end{aligned} \tag{A1}$$

Appendix B
Details of the Simulated Extreme Mass Ratio Inspiral Events

In this appendix, we first introduce the injection parameter configurations for three EMRIs (Table 3). Then, following the methodology of S. Babak et al. (2017), using Model M1 as the baseline, we calculate the total number of EMRI events (for Golden EMRIs) that could occur per year and evaluate the LISA detection rate for such events to be $10\,{\rm yr}^{-1}$. Although this study is based on a limited number of EMRI samples, which may pose certain limitations when generalizing to a broader population of LISA events, the results still clearly demonstrate the potential advantages of using galaxy cluster

Table 3
Injected Parameter Values for Configurations EMRI 1, EMRI 2, and EMRI 3

Parameter	EMRI 1	EMRI 2	EMRI 3
$\mu/M_{\odot}$	11.07	14.02	10.15
a	0.90	0.91	0.90
p_0/M	9.82	10.21	9.21
e_0	0.27	0.22	0.20
$\cos(I)_0$	0.98	0.56	0.69
d_L/Gpc	1.48	2.00	2.57
ϕ_S	4.04	2.87	0.49
θ_S	1.47	2.20	1.56
SNR	58.80	46.90	65.39
$\frac{\Delta d_L}{d_L}$	0.049	0.019	0.021
$\Delta\Omega/\mathrm{deg}^2$	3.36	3.52	5.65

Note. The injected parameter values of configurations EMRI 1, EMRI 2, and EMRI 3. The upper part of the table lists the specific injected parameter values and the corresponding SNR, while the lower part presents the measurement accuracy of the luminosity distance and the size of the sky localization area. Additionally, we fixed the values of the following parameters: $M = 10^6 M_{\odot}$, $\Phi_{\phi,0} = 2.0$, $\Phi_{\theta,0} = 3.0$, and $\Phi_{r,0} = 4.0$.

catalogs in the dark siren methodology (detailed results can be found in Section 4).

ORCID iDs

Wen-Biao Han https://orcid.org/0000-0002-2039-0726

References

Abbott, B. P., Abbott, R., Abbott, T. D., et al. 2016, PhRvL, 116, 061102
Abbott, B. P., Abbott, R., Abbott, T. D., et al. 2017a, PhRvL, 119, 161101
Abbott, B. P., Abbott, R., Abbott, T. D., et al. 2017b, Natur, 551, 85
Abbott, B. P., Abbott, R., Abbott, T. D., et al. 2017c, PhRvL, 119, 141101
Abbott, B. P., Abbott, R., Abbott, T. D., et al. 2021, ApJ, 909, 218
Abbott, R., Abe, H., Acernese, F., et al. 2023, ApJ, 949, 76
Alfradique, V., Bom, C. R., & Castro, T. 2025, arXiv:2503.18887
Amaro-Seoane, P., Audley, H., Babak, S., et al. 2017, arXiv:1702.00786
Amaro-Seoane, P., Gair, J. R., Freitag, M., et al. 2007, CQGra, 24, R113
Robitaille, T. P., Tollerud, E. J., et al. 2013, A&A, 558, A33
Astropy Collaboration, Price-Whelan, A. M., Lim, P. L., et al. 2022, ApJ, 935, 167
Astropy Collaboration, Price-Whelan, A. M., Sipőcz, B. M., et al. 2018, AJ, 156, 123
Auclair, P., Bacon, D., Baker, T., et al. 2023, LRR, 26, 5
Babak, S., Fang, H., Gair, J. R., Glampedakis, K., & Hughes, S. A. 2007, PhRvD, 75, 024005
Babak, S., Gair, J., Sesana, A., et al. 2017, PhRvD, 95, 103012
Ballard, W., Palmese, A., Hernandez, I. M., et al. 2023, RNAAS, 7, 250
Barack, L., & Cutler, C. 2004, PhRvD, 69, 082005
Berti, E., Sesana, A., Barausse, E., Cardoso, V., & Belczynski, K. 2016, PhRvL, 117, 101102
Bom, C. R., Alfradique, V., Palmese, A., et al. 2024, MNRAS, 535, 961
Chen, H.-Y., Fishbach, M., & Holz, D. E. 2018a, Natur, 562, 545
Chen, H.-Y., Fishbach, M., & Holz, D. E. 2018b, Natur, 562, 545
Chua, A. J. K., Katz, M. L., Warburton, N., & Hughes, S. A. 2021, PhRvL, 126, 051102
Chua, A. J. K., Moore, C. J., & Gair, J. R. 2017, PhRvD, 96, 044005
Feeney, S. M., Peiris, H. V., Nissanke, S. M., & Mortlock, D. J. 2021, PhRvL, 126, 171102
Finke, A., Foffa, S., Iacovelli, F., Maggiore, M., & Mancarella, M. 2021, JCAP, 2021, 026
Foreman-Mackey, D., Hogg, D. W., Lang, D., & Goodman, J. 2013, PASP, 125, 306
Freedman, W. L. 2017, NatAs, 1, 0169
Frieman, J. A., Turner, M. S., & Huterer, D. 2008, ARA&A, 46, 385
Gu, Y., Yang, X., Han, J., et al. 2024, MNRAS, 529, 4015
Hellinger, E. 1909, JRAM, 1909, 210
Hernandez, I. M., & Ray, A. 2024, arXiv:2404.02522
Holz, D. E., & Hughes, S. A. 2005, ApJ, 629, 15
Hu, W.-R., & Wu, Y.-L. 2017, NSRev, 4, 685
Jin, S.-J., Zhang, Y.-Z., Song, J.-Y., Zhang, J.-F., & Zhang, X. 2023, SCPMA, 67, 22
Karnesis, N., Katz, M. L., Korsakova, N., Gair, J. R., & Stergioulas, N. 2023, MNRAS, 526, 4814
Katz, M., CChapmanbird Speri, L., Karnesis, N., & Korsakova, N. 2024, ikekatz04/LISAanalysistools: First Main Release, v1.0.3, Zenodo, doi:10.5281/zenodo.10930980
Katz, M., Karnesis, N., & Korsakova, N. 2023a, mikekatz04/Eryn: First Full Release, v1.0.0, Zenodo, doi:10.5281/zenodo.7705496
Katz, M. L., Bayle, J.-B., Chua, A. J. K., & Vallisneri, M. 2022, PhRvD, 106, 103001
Katz, M. L., Chua, A. J. K., Speri, L., Warburton, N., & Hughes, S. A. 2021, PhRvD, 104, 064047
Katz, M. L., Speri, L., Chua, A. J. K., et al. 2023b, BlackHolePerturbationToolkit/FastEMRIWaveforms: Frequency Domain Waveform Added!, v1.5.1, Zenodo, doi:10.5281/zenodo.8190418
Klein, A., Barausse, E., Sesana, A., et al. 2016, PhRvD, 93, 024003
Laghi, D., Tamanini, N., Del Pozzo, W., et al. 2021, MNRAS, 508, 4512
Leandro, H., Marra, V., & Sturani, R. 2022, PhRvD, 105, 023523
Luo, J., Chen, L.-S., Duan, H.-Z., et al. 2016, CQGra, 33, 035010
Lyu, Z., Pan, Z., Mao, J., Jiang, N., & Yang, H. 2025, arXiv:2501.03252
MacLeod, C. L., & Hogan, C. J. 2008, PhRvD, 77, 043512
Muttoni, N., Laghi, D., Tamanini, N., Marsat, S., & Izquierdo-Villalba, D. 2023, PhRvD, 108, 23
Okuta, R., Unno, Y., Nishino, D., Hido, S., & Loomis, C. 2017, in Proc. of the Workshop on Machine Learning Systems (LearningSys), NeurIPS 2017 (San Diego CA: NeurIPS), 1, http://learningsys.org/nips17/assets/papers/paper_16.pdf
Palmese, A., Bom, C. R., Mucesh, S., & Hartley, W. G. 2023, ApJ, 943, 56
Perivolaropoulos, L., & Skara, F. 2022, NewAR, 95, 101659
Planck Collaboration, Aghanim, N., Akrami, Y., et al. 2020, A&A, 641, A6
Punturo, M., Abernathy, M., Acernese, F., et al. 2010, CQGra, 27, 194002
Reines, A. E., & Volonteri, M. 2015, ApJ, 813, 82
Reitze, D., Adhikari, R. X., Ballmer, S., et al. 2019, BAAS, 51, 35
Riess, A. G., Casertano, S., Yuan, W., et al. 2021, ApJL, 908, L6
Riess, A. G., Yuan, W., Macri, L. M., et al. 2022, ApJL, 934, L7
Rykoff, E. S., Rozo, E., Hollowood, D., et al. 2016, ApJS, 224, 1
Schutz, B. F. 1986, Natur, 323, 310
Soares-Santos, M., Palmese, A., Hartley, W., et al. 2019, ApJL, 876, L7
Stachurski, F., Messenger, C., & Hendry, M. 2024, PhRvD, 109, 5
Tamanini, N., Caprini, C., Barausse, E., et al. 2016, JCAP, 2016, 002
Ulmer, M. P., Adami, C., Durret, F., Ilbert, O., & Guennou, L. 2011, A&A, 528, A36
Venhola, A., Peletier, R. F., Salo, H., et al. 2021, arXiv:2111.01855
Virtanen, P., Gommers, R., Oliphant, T. E., et al. 2020, NatMe, 17, 261
Wen, Z. L., & Han, J. L. 2024, ApJS, 272, 39
Zhu, L.-G., Fan, H.-M., Chen, X., Hu, Y.-M., & Zhang, J.-d. 2024, ApJS, 273, 24